

SIMULATED AND EXPERIMENTAL INVESTIGATION OF MICROWAVE IMAGING USING UWB

A. Lazaro, D. Girbau, and R. Villarino

Department of Electronics, Electrics and Automatics Engineering
Universitat Rovira i Virgili (URV)
Av. Països Catalans 26, Campus Sescelades, Tarragona 43007, Spain

Abstract—Microwave breast tumour detection is a non-invasive technique that uses non ionizing radiation. Microwave imaging has the potential to achieve early detection of breast cancer due to the high specificity and the large difference in electrical properties of the malignant tissue when compared to normal breast tissue. This paper studies the feasibility of using UWB signals for breast imaging. Simulated results using Finite-Difference Time-Domain (FDTD) Method will be presented. A sensibility study of the variations in the breast relative dielectric permittivity and of the variations of the skin-surface contour is also provided. A working prototype for microwave imaging is developed using a conventional Vector Network Analyzer (VNA) with the time processing capability.

1. INTRODUCTION

Nowadays, the main technique used in breast cancer detection consists in X-rays mammogram. However, this technique presents some problems such as the use of ionizing radiation, the breast compression and the difficulty of its application on young women [1]. Microwave imaging is an alternative to X-rays [1, 2]. The early-tumour detection principle is based on the analysis of the differences in the dielectric properties between the healthy and malignant tissues [3]. On the other hand, there has been a recent expansion of several techniques based on Ultra-Wide Band (UWB) pulses, especially for communication systems, which are also interesting for tomography applications [2–5].

Although some simulated feasibility studies have been reported in the literature [2, 4–7], small experimental results can be found using

Corresponding author: A. Lazaro (antonioramon.lazaro@urv.cat).

UWB-like techniques [2, 4, 8–10]; moreover, some clinical tests have been performed using UWB [11, 12] and other techniques [13]. In this paper, a Vector Network Analyser (VNA) and a UWB antenna are used to illuminate the target and collect the reflected signals. The time-domain signals are obtained by means of the inverse Fourier Transform. This measurement setup is easier to implement in a laboratory rather than specific UWB radar-based setups, since it uses general-purpose microwave instrumentation (VNA).

Several UWB antenna topologies have been proposed for breast detection [14–16] and also Wireless Body-Area Networks [16]. Among UWB antenna design in the recent literature, the monopole planar antenna is widely used due to its wide bandwidth, simple structure and low cost; it has become one of the most considerable candidates for UWB applications. The UWB monopole antenna has a low number of design parameters, higher efficiency and easier fabrication than resistive antennas for tomography proposed in the literature [9]. Moreover, in [17], the UWB disc monopole has demonstrated good return loss and electromagnetic absorption in human body. Consequently, in this experiment a UWB disc monopole has been designed using the method of moments implemented in the Agilent Momentum. The antenna has been chosen to be broadband in order to optimize the penetration depth and to limit the attenuation of the transmitted signal. High frequencies are advantageous for detecting tumors near the skin, whereas low-frequency waves are beneficial for detecting tumors at deeper locations. Here, the high-frequency limit is determined by the VNA (3 GHz). The low-frequency limit is determined by the antenna dimensions and it is chosen to be 0.5 GHz.

In most experiments for tumor detection, the breast and the antenna are immersed in a dielectric medium such as soybean oil ($\epsilon_r = 2.6$, $\sigma = 0.05$ S/m at 6 GHz) [9], canola oil [18] ($\epsilon_r = 2.5$, $\sigma = 0.04$ S/m at 6 GHz), corn syrup ($\epsilon_r = 18.9$ – 56.9 , $\sigma = 0.3$ – 2.2 S/m) [19] or other liquids which have a dielectric constant similar to that of the skin [4, 9]. Hence the antenna will be well matched. However skin and breast permittivities can change from one patient to other and a residual reflection at the skin should be expected. Sometimes, breast immersion can be difficult and it can be annoying for the person.

In this experiment a *phantom* has been designed in order to simulate the scene (see Figure 1). A low-permittivity rod is used to simulate the tumor. The rod is immersed in a water-filled cylindrical glass tank. The skin is simulated using the cylindrical surface of the tank and the antenna is air coupled [10]. Thus, important reflections are expected from the skin. Hence a high mismatch between air and

skin simplifies the detection of the breast contour. In addition to this, the dielectric permittivity and losses of water are considerably higher than in a real breast and it can be considered as a worst case for processing algorithms due to the higher attenuation of water and the reflection in the air-to-skin interface. Moreover, due to these high permittivities, the resolution (related to the wavelength) obtained with this system is expected to be comparable with other experiments proposed where higher frequencies had been used (up to 10 GHz in [9]).

Since the antenna pattern is not directive, several reflections from surrounding objects are collected. From this point of view, it is a good scene to check the clutter reduction and skin removal algorithms that have been used. The skin and breast permittivity may also change from one person to the other and a residual reflection on the skin should be expected. Measurements are done in reflection (the same antenna transmits and records the reflections). To create a synthetic array, the antenna is physically scanned to different locations describing a circle and measurements are repeated at each location.

The paper is organized as follows. The microwave imaging recovery algorithm is described in Section 2. Two skin-breast artifact removal methods are compared: the background subtraction and the Wiener filter. The performance of the calibration and focusing algorithms are compared by using synthetic measures obtained from Finite-Difference Time-Domain (FDTD) simulations. A sensibility study of the variations in the breast relative dielectric permittivity and of the variations of the skin-surface contour is also presented.

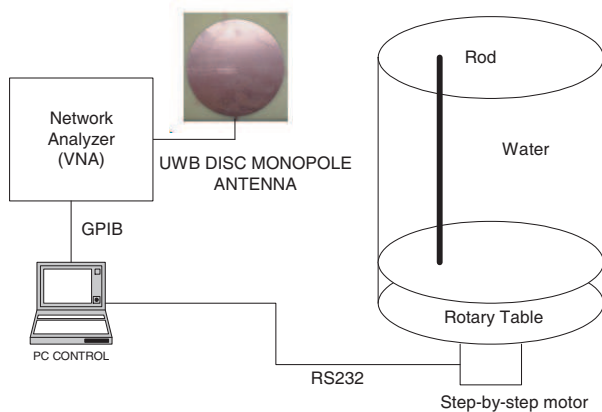


Figure 1. Experimental setup.

In Section 3, experimental results are presented. Finally, Section 4 summarizes the work.

2. MICROWAVE IMAGING ALGORITHM

Microwave imaging consists in transmitting a pulse and receiving the reflected signal at an antenna array located around the area of analysis. The received signal $s_i(t)$ at the antenna i is the sum of all the pulses $p(t)$ reflected at the objects placed in the scene and attenuated due to the propagation through the different paths:

$$s_i(t) = \sum_{j=1}^N \alpha_{ij} R_{ij} p(t - \tau_{ij}) \quad (1)$$

where R_{ij} and α_{ij} are the reflectivity and the attenuation at each point r_j , and τ_{ij} is the signal propagation delay from the transmitting to the receiving antenna i , caused by the reflection produced at the r_j point.

The imaging basic principle is based on the confocal technique (also known as time-shift-and-add algorithm) [2]. It consists in overlapping the signals reflected on a test point r_j delayed by a time delay equal to the propagation time τ_{ij} . If r_j is a high-reflectivity point, the overlapped signals received at every antenna will yield a high value. On the contrary, if the reflectivity is poor, the value will be low due to the finite pulse duration. Before adding the signals, a weighting factor is applied to each signal to compensate the attenuation due to

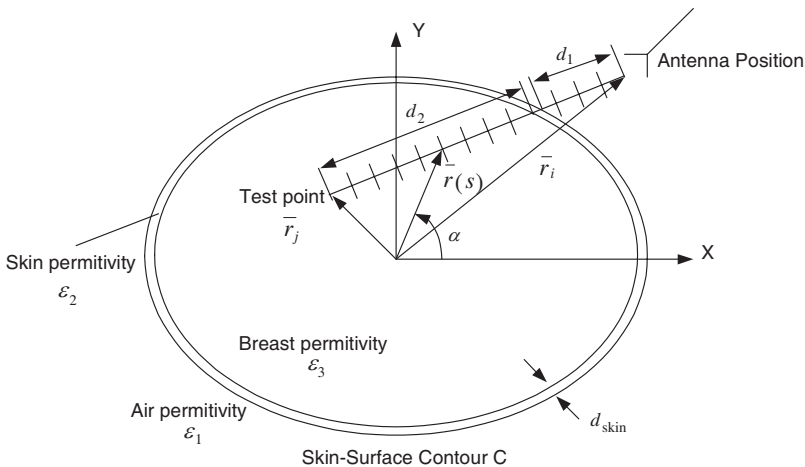


Figure 2. Phantom schema showing the skin-surface contour.

propagation. This algorithm is performed for each focal point r_j in the scene. Since (1) is a first-order model, the multiple reflections between objects and different tissue layers are neglected. These simplifications are equivalent to the ones performed in the *Born* approximation which are applied in diffraction tomography techniques [20]. In addition, in time domain, multiple reflections between scatters can be filtered most of the times by selecting a suitable time window.

As already introduced, the scene configuration proposed in this work (*phantom*) consists of a water-filled cylindrical glass tank with a sample rod inside. The antenna is located outside, in contrast with other works [2, 4, 9] that put the antennas inside of a gel or in an environment with a dielectric permittivity similar to the *phantom*. In consequence, a strong reflection between the glass surface and the air is expected, and the real reflection between skin and air is better emulated.

An important issue is the calculation of the propagation delay τ_{ij} (see Figure 2). The skin-surface can be obtained from the interpolation of the skin-surface contour, which is estimated from the peak delay using the algorithm proposed in [8]. A similar algorithm is applied in ground penetrating radar (GPR) to obtain the contour of buried objects [21]. The contour surface can also be estimated using other mechanical or optical procedures. In consequence, it is assumed that the skin-surface contour (C) of the phantom is known and given by a table of points $r_C(\alpha)$, where α is the angle with respect to the X axis. For simplicity, only the points inside the breast delimited by the skin surface are reconstructed. The delay τ_{ij} , assuming a monostatic topology is calculated using:

$$\tau_{ij} = \frac{2d_1}{c/\sqrt{\varepsilon_{r1}}} + \frac{2d_{skin}}{c/\sqrt{\varepsilon_{r2}}} + \frac{2d_2}{c/\sqrt{\varepsilon_{r3}}} \quad (2)$$

where c is the light velocity ($c = 3 \cdot 10^8$ m/s), d_1 is the distance between the antenna position r_i and the outer skin-surface, d_{skin} is the skin thickness and d_2 is the distance between the inner skin surface and the test point r_j ($d_2 = |r_j - r_i| - d_1 - d_{skin}$). ε_{r1} , ε_{r2} and ε_{r3} are the relative dielectric permittivities of the air, skin and breast, respectively.

The algorithm to calculate the distance d_1 is as follows. The line that joins the points r_i and r_j is divided into arbitrary short segments (typically shorter than $\lambda_{air}/100$, where λ_{air} is the wavelength in air). The end point of each segment is given by the line equation:

$$\bar{r}(s) = \bar{r}_i + s \cdot (\bar{r}_j - \bar{r}_i) \quad (3)$$

where s is a parameter which ranges from 0 to 1. Then, it is checked for each segment end point $r(s)$ whether it is inside or outside of the

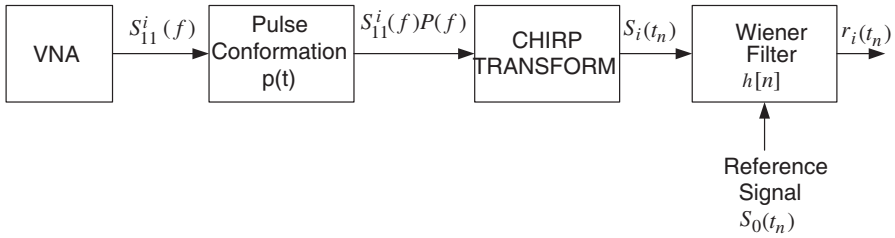


Figure 3. Block diagram of the time signal calibration process.

skin-surface contour. A simple search allows determining the segment that intercepts the skin-surface contour. To check if a point with polar coordinates $r(\alpha)$ is inside the contour, the radial distance r between the point and the radial distance from the centre to contour surface in direction of the point, $r_C(\alpha)$, are compared. If $r < r_C(\alpha)$, the point is inside the contour.

The next step is system calibration, also known as skin-breast artifact removal (see Figure 3). To this end, the following components from the time signal have to be removed: 1/ the reflections in the scene objects that do not intervene on the analyzed sample, 2/ the antenna time response and 3/ the reflections between air and the glass cylinder. Calibration can be done by measuring the time response without the sample (clutter or background) and subtracting it from the measured signal (now with the rod) at each angular position. This technique is known as background subtraction. However, this technique does not correct the effect of skin reflections. A more appropriated method consists in subtracting the average value at each angular position since, if the contributions to the signal that are common to all angular positions do not depend on the rod, these would compensate themselves. In this case, instead of subtracting the average value of the signals, the weighted average is subtracted. This can be implemented by means of a *Wiener* filter [8]. The output of the filter yields:

$$y[n] = \sum_{i=1}^N s_i[n] \cdot h[i] \quad (4)$$

From a reference signal (which can be the measurement at one of the angular positions, $s_0(t)$), the FIR filter coefficients $h[n]$ are obtained in order to minimize the mean square error between its output and the reference signal. The filter coefficients $h[n]$ are the components of the following vector:

$$\bar{h} = \text{pinv}([\bar{s}_1 \ \bar{s}_2 \ \dots \ \bar{s}_M]) \cdot \bar{s}_0 \quad (5)$$

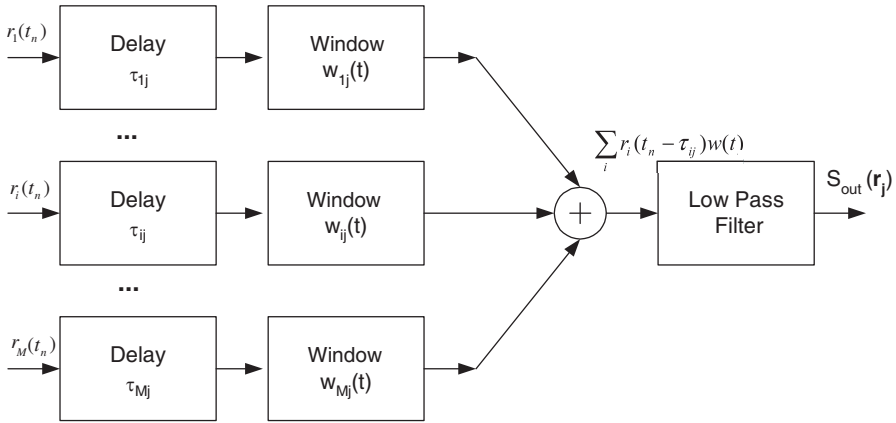


Figure 4. Focusing process.

where \bar{s}_i is a column vector composed of samples of the time signal for the angular position i and $pinv$ is the pseudo-inverse matrix obtained from its decomposition in singular values (SVD) [21]. The calibrated signal $r_i(t)$ for each angular position at every sampling time t_n is:

$$r_i[n] = s_i[n] - y[n] = s_i[n] - \sum_{i=1}^N s_i[n]h[i] \quad (6)$$

As already introduced, the focusing process (see Figure 4) consists in delaying the signal of every antenna a quantity equal to the predicted propagation delay (τ_{ij}) between the antenna and the point to be recovered. Then, the delayed signals are overlapped and the result is time averaged over the pulse duration around each point using a low-pass filter. Since the signals belong to the discrete domain, the delay is applied by means of an interpolation process.

The design and the analysis of the scattering observed in high-contrast objects are carried out by using the Finite-Difference Time-Domain (FDTD) method [19]. The response of 32 antennas uniformly distributed around a simulated breast is obtained. A 10 GHz-bandwidth *ricker* pulse (*Gaussian* derived pulse) was injected. The antennas are uniformly distributed in a 6 cm-radius circumference around the breast and are not immersed in any gel. An elliptical surface is simulated to better evaluate the calibration algorithm. Permittivity values of skin and of healthy and malignant tissues were taken from [3] (see Table 1). The permittivity expression (7), known as Cole-Cole model, includes a frequency-dispersion model and takes into account

typical conductivities. The simulated tumour is emulated by a 5 mm diameter rod.

$$\varepsilon_{rc} = \varepsilon_r(\infty) + \frac{\varepsilon_r(0) - \varepsilon_r(\infty)}{1 + j\omega\tau} + \frac{\sigma}{j\omega\varepsilon_0} \quad (7)$$

In (7), $\varepsilon_r(0)$ and $\varepsilon_r(\infty)$ are the DC and high-frequency relative permittivities, respectively, σ the conductivity and τ the constant that controls frequency dispersion.

Figure 5 shows the reflectivity image by using the background subtraction algorithm. The mean Signal-to-Clutter Ratio (S/C) is defined as the ratio between the mean energy within the malign area (known in the case of simulations and estimated from peak energy in the case of measurement with phantoms) to the mean energy outside the malign area, known as clutter. The mean Signal-to-Clutter Ratio (S/C) achieved between the malignant and the healthy tissue is 22 dB. Figure 6 presents the same image, although in this case the Wiener-filter skin-breast artifact removal algorithm is used. It can be observed that in this case the skin measurement has not been removed due to the elliptic shape; although S/C decreases down to 15 dB, the malignant tissue is much clearer than in the previous case.

The dependence on the number of antennas has been studied when using the Wiener-filter skin-breast artifact removal algorithm. Figure 7 shows the focusing algorithm output at the centre of the malignant tissue, which has been placed at the centre of the scene. For high-reflectivity regions, the value increases quadratically with the number of antennas, whereas for low reflectivity regions this value is

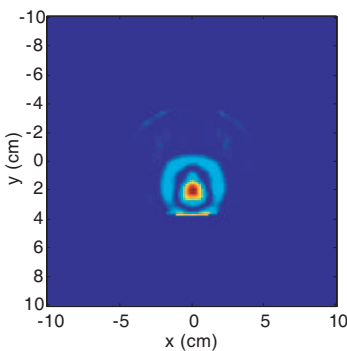


Figure 5. Reflectivity image by using the background subtraction algorithm (S/C = 22 dB).

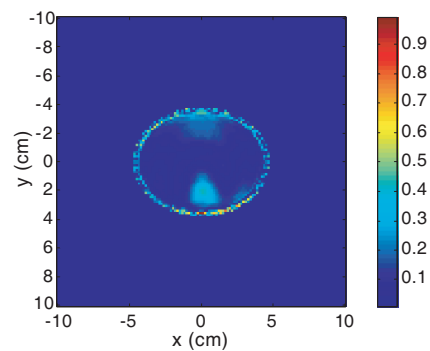


Figure 6. Reflectivity image by using the Wiener-filter skin-breast artifact removal algorithm. (S/C = 15.45 dB).

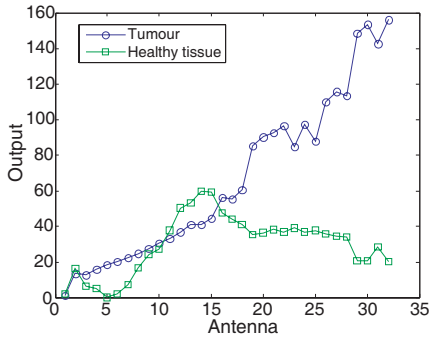


Figure 7. Focusing algorithm output level for a healthy tissue and a tumour as a function of the antenna number.

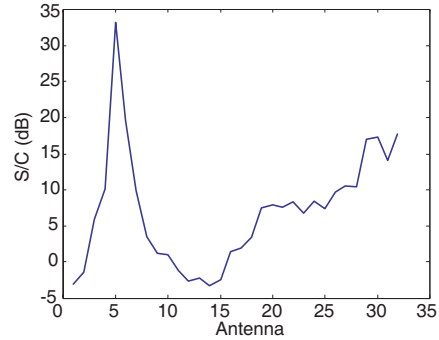


Figure 8. S/C between malignant and healthy tissue as a function of the antenna number.

Table 1. Permittivity parameters used in the permittivity model (7).

Tissue	$\epsilon_r(\infty)$	$\epsilon_r(0)$	$\sigma(\text{S/m})$	$\tau(\text{ps})$
Skin	4	37	1.1	7.23
Normal	7	10	0.15	7
Malignant	3.99	54	0.7	7

approximately constant when more than 15 antennas are considered and decreases if the number of antennas is under 15. Figure 8 shows the S/C between a malignant and a healthy tissue as a function of the number of antennas. The S/C tends to a stable value when the antenna number is high, reaching the mean S/C of the scene.

Breast permittivity changes from one person to the other, since it depends on the level of water in the tissue. This permittivity has to be known for calculation of the delay τ_{ij} (2). A characterization of breast permittivity can be done by using techniques based on microwave probes [3, 24, 25]. The sensitivity of the imaging methods to small variations in the breast permittivity (for instance, due to measurement uncertainties) is here evaluated. To this end, both calibration methods have been applied to the previous simulations (with the nominal breast permittivity), but now assuming a variation in the nominal breast permittivity.

Table 2 resumes the S/C obtained for each calibration method. Figures 9 and 10 show the results after the background subtraction

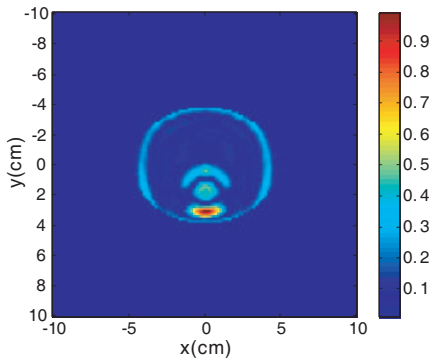


Figure 9. Reflectivity image by using the background subtraction algorithm with a variation of 25% in the permittivity ($S/C = 14.49$ dB).

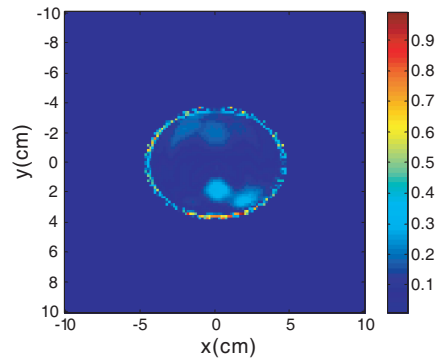


Figure 10. Reflectivity image by using the Wiener-filter skin-breast artifact removal algorithm with a variation of 25% in the permittivity ($S/C = 12.80$ dB).

Table 2. Sensitivity of the mean Signal-to-Clutter Ratio (S/C) to the change in permittivity of the breast as a function of the calibration method.

Variation of Permittivity %	Calibration method	
	Background Subtract	Skin-breast artifact removal
5	21.34	15.45
10	20.10	15.15
15	18.70	14.62
20	16.98	13.84
25	14.49	12.80
30	10.84	11.43
35	7.40	9.65

and Wiener-filter skin-breast artifact removal algorithms are applied, assuming a variation of 25% in the nominal breast permittivity. These results show that a variation in the breast permittivity introduces an error in the determination of time delays (2), and thus, in the confocal image. The effect in both methods is the presence of a false high-reflectivity region close to the tumor. The reflectivity of this region increases with the variation of the permittivity, reducing the S/C ratio. In the case of background subtraction this region appears due to the

reflection of the pulse at the inner skin surface. This effect is also shown in Figure 5, but there the location is close to the skin surface. Now, when variations in the breast permittivity are present, its location is shifted to the interior. Finally, it has been noted that the variation in the breast permittivity does not affect the elimination of the antenna response and skin reflection.

Another error source in the imaging methods is the sensitivity to variations in the contour, which are here studied. Using the FDTD for the scene of Figures 5–6 (with an elliptic contour of 5 cm for X -axis and 4 cm for Y -axis) the imaging method has been applied for a wrong contour estimation (two circular contours with radius of 4 cm and 5 cm). Figures 11 and 12 show the reflectivity images after the background algorithm and the focusing procedure for the two circular contours are applied. Figures 13 and 14 show the reflectivity images after the Wiener-filter skin-breast artifact algorithm and the focusing procedure for the two circular contours are applied. When the assumed contour is larger than the real contour (case with radius 5 cm), the reduction in the S/C ratio is moderate. In addition, in case of background subtraction, the real skin contour is visible. This effect can be used to obtain a better estimation of the skin contour. When the Wiener filter is used, an increase of clutter near the skin surface is obtained (see Figures 13 and 14). On the contrary, if the assumed contour is smaller than the real contour (case with radius 4 cm), the error increases for the two calibration methods. Due to the higher permittivity of the breast compared to the air, the error produced by an increase in the inner propagation distance (d_2) is smaller than the error in the air distance (d_1).

3. EXPERIMENTAL RESULTS

The experimental setup (see Figure 1) consists of a 0.5 to 3 GHz UWB antenna connected to the vector network analyzer (VNA). The scene consists of a rod (emulating the malignant tissue) located into a 10-cm diameter water-filled glass cylindrical tank which rotates with respect to its centre axis by means of a step-by-step motor; hence, it is equivalent to a cylindrical antenna array. The $S_{11}^i(f)$ parameter is measured for each position between 0.5 GHz and 3 GHz. The signal spectrum is multiplied by a derived *Gaussian* pulse and then, the *Chirp* Transform is applied to obtain the time signal. A *Hamming* window is applied to the signal to decrease the effect of the finite bandwidth during the inverse transform process. *Chirp* Transform is selected instead of Fast *Fourier* Transform (FFT) because with this method the time resolution does not depend on the number of measured samples

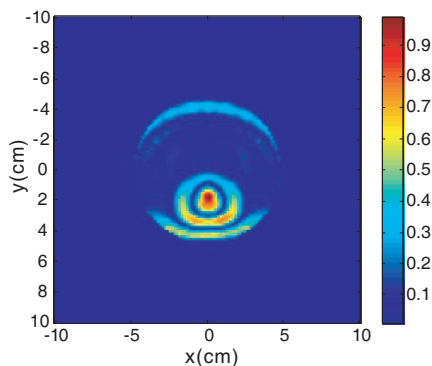


Figure 11. Reflectivity image by using the background subtraction algorithm and a circular contour of radius 5 cm ($S/C = 18.38$ dB).

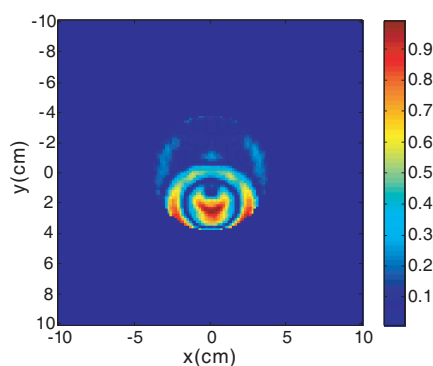


Figure 12. Reflectivity image by using the background subtraction algorithm and a circular contour of radius 4 cm ($S/C = 16.38$ dB).

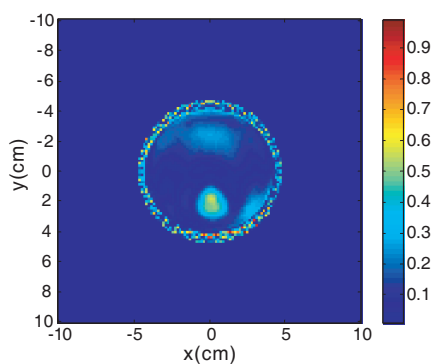


Figure 13. Reflectivity image by using the Wiener-filter skin-breast artifact removal algorithm and a circular contour of radius 5 cm ($S/C = 14.98$ dB).

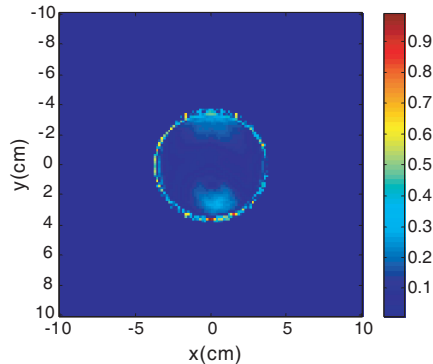


Figure 14. Reflectivity image by using the Wiener-filter skin-breast artifact removal algorithm and a circular contour of radius 4 cm ($S/C = 11.43$ dB).

in the frequency domain.

Figure 15 shows the S_{11} parameters measured from 0.5 to 3 GHz for 72 angular positions. The diameter of the rod is 4 mm. Since attenuation in water increases rapidly with frequency, more fluctuations are observed in the region under 1.5 GHz, as expected. Figure 16 shows the measured time response (original signal) and the signal after the calibration algorithm is applied. It can be observed

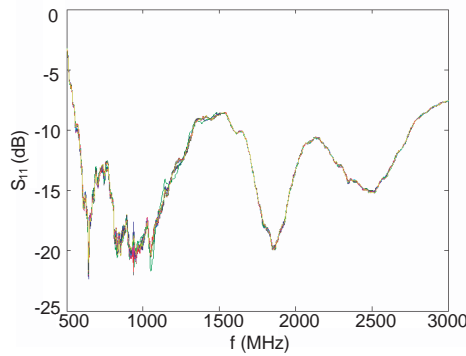


Figure 15. (a) Original signals as a function of time and angular positions, (b) signals after the calibration algorithm is applied.

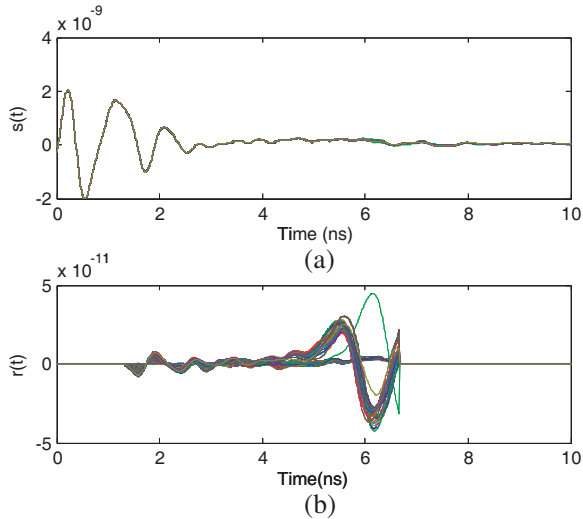


Figure 16. Measured reflectivity image for a 4 mm-diameter rod using the Wiener filter skin-breast artifact removal algorithm. ($S/C = 16.5$ dB).

that variations due to reflections at the cylinder and at distant objects are enhanced. However, the latter is ignored by the focusing algorithm, since they correspond to longer delays than the ones considered in the reconstruction area.

Figure 17 shows the measured reflectivity image using the Wiener filter skin-breast artifact removal algorithm. The mean S/C ratio

between the cylinder and the rest of the scene is 16.5 dB. A shadow close to the position of the sample is observed.

Figure 18 shows the measured reflectivity image of a 1-cm diameter rod placed 2.5 cm away from the centre of the glass cylinder using the Wiener-filter skin-breast artifact removal algorithm. The mean S/C ratio is 14.2 dB. Figure 19 shows the measured reflectivity image when the background subtraction algorithm is applied. Results are not better than in the previous case (Figure 18). Even the S/C ratio is slightly lower (S/C = 13.8 dB). The measured S/C using

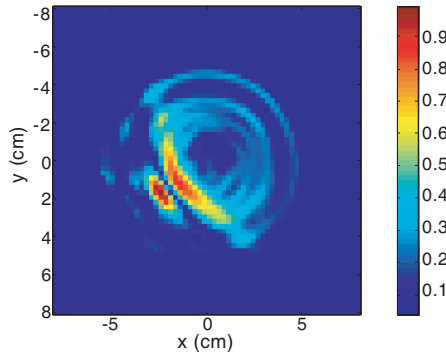


Figure 17. Measured reflectivity image for a 10 mm-diameter rod using the Wiener filter skin-breast artifact removal algorithm. (S/C = 14.2 dB).

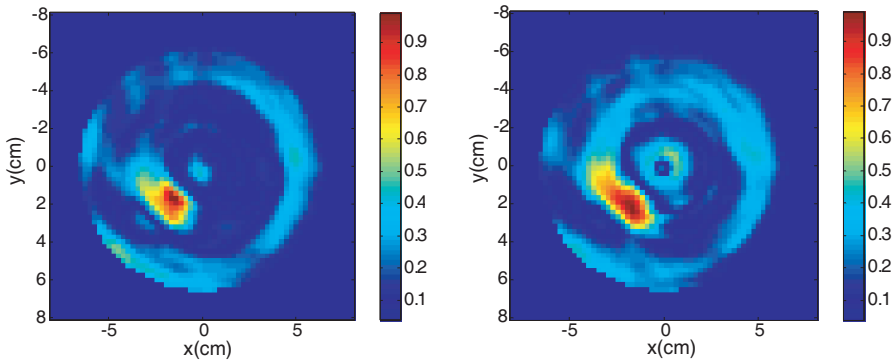


Figure 18. Measured reflectivity image for a 10-mm diameter rod using the Wiener-filter skin-breast artifact removal algorithm (S/C = 14.2 dB).

Figure 19. Measured reflectivity image for a 10-mm diameter rod using the background subtraction algorithm (S/C = 13.8 dB).

these *phantoms* is very similar to the S/C obtained in the previous simulations performed with typical tissue parameters.

4. CONCLUSION

In this paper, a feasibility study of microwave imaging for breast tumor detection using UWB has been presented. The system is based on the frequency measurement of the reflection coefficient with a VNA and an air-coupled UWB antenna between 0.5–3 GHz. A comparison between two skin-breast artifact removal algorithms, background subtraction and *Wiener* filter, to eliminate the antenna response and the skin reflections has been done. A simple formulation for the Wiener filter using the pseudoinverse matrix has been derived. The two skin-breast artifact removal algorithms have been validated by FDTD simulation and by measuring *phantoms*. Since water (with high losses and dielectric permittivity) has been used in the *phantoms* and the antennas have been air coupled (with the consequent high reflection in the interface *phantom-air*), this can be considered a worst-case study. Signal-to-Clutter (S/C) ratios between malignant and healthy tissues obtained from measurements are in the order of the values obtained from simulation. Similar S/C ratios have been obtained using the two algorithms.

The sensitivity to changes in the breast permittivity and the skin-surface contour has been investigated. Changes in the breast permittivity of 25% can be tolerated for both calibration methods with a S/C reduction of about 6.5 dB for the background subtraction and 2.7 dB for the Wiener-filter skin-breast artifact removal algorithm. The main effect of uncertainty in the breast permittivity is the possible presence of high-reflectivity regions (with an aspect similar to a tumor). The reflectivity of these regions increases with the breast permittivity variation. As a conclusion, a good estimation of breast permittivity within the range 25–30% is required. This point could be a serious drawback, since the permittivity changes from one person to the other, depending on the level of water in the breast tissue. In consequence, a characterization of breast permittivity using techniques based on microwave probes could be needed before the focusing algorithms are applied.

Another important issue is the determination of skin-surface contour. Although the antennas may be immersed in a liquid or material with similar permittivity to that of the breast, the skin-surface contour must be measured or estimated. In this work it has been studied the effect of a rough estimation of the skin contour. In case of using air-coupled antennas, the high reflection coefficient

between air and skin can help to estimate the skin contour, by using techniques such as the ones proposed in [8,21]. It has been found that if a rough estimation of the contour is used, the position of the tumor is detected with a reasonable reduction of S/C in both algorithms, especially in the Wiener-filter skin artifact algorithm where the reduction is less than 1.5 dB. The results are better if the estimated skin-surface contour is larger than the real contour, but not the other way round, since the errors in the propagation delay used in the confocal algorithm are smaller. In this case a rough estimation of the skin contour larger than the real contour could be combined with the background subtraction algorithm to estimate a new contour (that could be simply determined graphically from the image or using edge-detection processing techniques). Using this new contour estimation, with either background subtraction or Wiener-filter skin-breast artifact removal, better tumor detection could be carried out.

ACKNOWLEDGMENT

This paper was supported by the Spanish Government Project TEC2008-06758-C02-02.

REFERENCES

1. Fear, E. C., P. M. Meaney, and M. A. Stuchly, "Microwaves for breast cancer detection?" *IEEE Potentials*, Vol. 22, No. 1, 12–18, 2003.
2. Fear, E. C., J. Sill, and M. A. Stuchly, "Experimental feasibility study of confocal microwave imaging for breast tumour detection," *IEEE Trans. Microwave Theory and Tech.*, Vol. 51, No. 3, 887–892, 2003.
3. Hagl, D. M., D. Popovic, S. C. Hagness, J. H. Booske, and M. Okoniewski, "Sensing volume of open-ended coaxial probes for dielectric characterization of breast tissue at microwave frequencies," *IEEE Trans. Microwave Theory and Tech.*, Vol. 51, No. 4, 1194–1206, 2003.
4. Bindu, G., S. J. Abraham, A. Lonappan, V. Thomas, C. K. Aanandan, and K. T. Mathew, "Active microwave imaging for breast cancer detection," *Progress In Electromagnetics Research*, PIER 58, 149–169, 2006.
5. Zhang, H., S. Y. Tan, and H. S. Tan, "A novel method for microwave breast cancer detection," *Progress In Electromagnetics Research*, PIER 83, 413–434, 2008.

6. Bond, E. J., X. Li, S. C. Hagness, and B. D. Van Veen, "Microwave imaging via space-time beamforming for early detection of breast cancer," *IEEE Trans. on Antennas and Propagation*, Vol. 51, No. 8, 1690–1705, 2003.
7. Zainud-Deen, S. H., W. M. Hassen, E. M. Ali, K. H. Awadalla, and H. A. Sharshar, "Breast cancer detection using a hybrid finite difference frequency domain and particle swarm optimization techniques," *Progress In Electromagnetics Research B*, Vol. 3, 35–46, 2008.
8. Li, X., E. J. Bond, B. D. Van Veen, and S. C. Hagness, "An overview of ultra-wideband microwave imaging via space-time beamforming for early-stage breast-cancer detection," *IEEE Antennas and Propagation Magazine*, Vol. 47, No. 1, 19–34, 2005.
9. Sill, J. M. and E. C. Fear, "Tissue sensing adaptive radar for breast cancer detection — Experimental investigation of simple tumor models," *IEEE Trans. on Microwave Theory and Tech.*, Vol. 53, No. 11, 3312–3319, 2005.
10. Zhou, H., T. Takenaka, J. Johnson, and T. Tanaka, "A breast imaging model using microwaves and a time domain three dimensional reconstruction method," *Progress In Electromagnetics Research*, PIER 93, 57–70, 2009.
11. Klemm, M., I. Craddock, J. Leendertz, A. Preece, and R. Benjamin, "Experimental and clinical results of breast cancer detection using UWB microwave radar," *IEEE Antennas and Propagation Society International Symposium, AP-S 2008*, 1–4, 2008.
12. Craddock, I. J., M. Klemm, J. Leendertz, A. W. Preece, and R. Benjamin, "An improved hemispherical antenna array design for breast imaging," *Proceedings European Conference on Antennas and Propagation, EuCAP 2007*, 1–5, 2007.
13. Meaney, P. M., M. W. Fanning, D. Li, S. P. Poplack, and K. D. Paulsen, "A clinical prototype for active microwave imaging of the breast," *IEEE Transactions on Microwave Theory and Techniques*, Vol. 48, No.11, 1841–1853, 2000.
14. Kanj, H. and M. Popovic, "A novel ultra-compact broadband antenna for microwave breast tumor detection," *Progress In Electromagnetics Research*, PIER 86, 169–198, 2008.
15. Amineh, R. K., A. Trehan, and N. K. Nikolova, "TEM horn antenna for ultra-wide band microwave breast imaging," *Progress In Electromagnetics Research B*, Vol. 13, 59–74, 2009.
16. Lim, K.-S., M. Nagalingam, and C.-P. Tan, "Design and construction of microstrip UWB antenna with time domain

- analysis,” *Progress In Electromagnetics Research M*, Vol. 3, 153–164, 2008.
17. Klemm, M. and G. Troester, “EM energy absorption in the human body tissues due to UWB antennas,” *Progress In Electromagnetics Research*, PIER 62, 261–280, 2006.
 18. Li, X., S. K. Davis, S. C. Hagness, D. W. van der Weide, and B. D. Van Veen, “Microwave imaging via space time beamforming: Experimental investigation of tumor detection in multilayer breast phantoms,” *IEEE Trans. Microwave Theory and Tech.*, Vol. 52, 1856–1865, August 2004.
 19. Bindu, G., A. Lonappan, V. Thomas, C. K. Aanandan, and K. T. Mathew, “Dielectric studies of corn syrup for applications in microwave breast imaging,” *Progress In Electromagnetics Research*, PIER 59, 175–186, 2006.
 20. Slaney, M. and A. C. Kak, “Limitations of imaging with first-order diffraction tomography,” *IEEE Trans. Microwave Theory and Tech.*, Vol. 32, No. 8, 860–874, 1984.
 21. Sakamoto, T. and T. Sato, “A target shape estimation algorithm for pulse radar systems based on boundary scattering transform,” *IEICE Trans. Commun.*, Vol. E87-B, No. 5, 1357–1365, 2004.
 22. Golub, G. H. and C. F. Van Loan, *Matrix Computations*, 3rd edition, Johns Hopkins, ISBN 978-0-8018-5414-9, 1996.
 23. GprMAX V2.0, available in www.gprmax.org.
 24. Zajíček, R., T. Smejkal, L. Oppl, and J. Vrba, “Medical diagnostics using reflection method and waveguide probes—feasibility study,” *PIERS Proceedings*, 759–762, Cambridge, USA, July 2–6, 2008.
 25. Zajíček, R., L. Oppl, and J. Vrba, “Broadband measurement of complex permittivity,” *Radioengineering*, Vol. 17, No. 1, 14–19, 2008.